Renewable Energy
April 2024, Volume 224 Pages 120107 (9p.)
https://doi.org/10.1016/j.renene.2024.120107
https://archimer.ifremer.fr/doc/00876/98822/

On the necessity of considering the hub when examining the induction of a horizontal axis tidal turbine

Druault Philippe [1, *], Krawczynski Jean-François [1], Çan Erdi [1], Germain Gregory [2]

[1] Sorbonne Université, CNRS, Institut Jean Le Rond d'Alembert, F-75005 Paris, France
[2] Ifremer, Marine Structure Laboratory, 150 quai Gambetta, 62200 Boulogne-sur-mer, France

* Corresponding author : Philippe Druault, email address : philippe.druault@sorbonne-universite.fr

Abstract :

The induction models developed for wind turbines are not suitable for tidal turbines. The main reason is related to the differences in the ratio of the hub diameter to the rotor diameter, much more important in the case of tidal turbines. Thus, the hub contribution cannot be ignored. Furthermore, the specificities of the flow that impacts the turbine (strong shear) have to be taken into account contrary to a supposedly uniform upstream flow. To address these challenges, a new analytical induction model is proposed that combines both models related to the rotating blade and the hub effect. The effectiveness of the new model is evaluated against a specific experimental database for which a scale horizontal axis tidal turbine is placed in several representative turbulent shear flows. Particle Image Velocimetry measurements are synchronized with turbine thrust measurements to analyze the modifications of the mean velocity fields as a function of the thrust coefficient. The comparison shows that, regardless of the turbine rotational speed and/or the nature of the incoming shear velocity profile, the new model is in good agreement with the experimental results. Therefore, this result is very important for numerical modeling of the flow around the tidal turbines.

Highlights

► Tidal turbine blockage analysis for various thrust values and incoming shear flows. ► Modified wind turbine induction model for large hub-to- turbine diameter ratio. ► Development of a hybrid analytical tidal turbine induction model. ► The model separately considers the action of the hub and the rotating blades. ► The new model and experimental data showed good agreement regardless of turbine speed.

Keywords : Induction analytical model, tidal turbine, shear flow

1. Introduction

The presence of a rotating turbine in a flow produces a region of considerably reduced flow velocity downstream of the rotor (the wake) and a region of reduced flow velocity upstream (the induction zone). The induction effects alter the properties of the incoming flow up to several diameters upstream in both the wind (Medici et al., 2011; Simley et al., 2016; Bastankhah and Porte-Agel, 2017) and the tidal (Druault and Germain, 2022; Jouenne et al., 2023) turbine contexts. A comprehensive understanding of incoming flow dynamics is essential to improve device design, turbine array reliability, and ultimately energy conversion rate. Indeed, recent studies show that it is important to consider the impact of global wind or tidal farm blockage to improve the prediction accuracy of turbine power output (Branlard and Meyer Forsting, 2020; Segalini, 2021; Meyer Forsting et al., 2023; Zhang et al., 2023) Keane et al. (2022) also show that the cumulative induction zone effect of wind turbines results in a reduction in both the induction zone wind velocity and the corresponding reduction in energy yield. The same effects are expected for tidal turbines. It is therefore essential to study these effects to ensure the farms development and to obtain a more accurate estimate of the flow affecting each turbine in the farm.

From a numerical point of view, several models allow the mean axial velocity deficit ahead of a horizontal axis wind turbine (HAWT) to be estimated as well as the global mean velocity field in a wind farm (Branlard and Gaunaa, 2015; Sorensen, 2016; Troldborg and Meyer Forsting, 2017; Branlard and Meyer Forsting, 2020; Segalini, 2021). It was shown both numerically and experimentally that they provided a good approximation of the modification of the mean axial velocity upwind of a wind turbine (Medici et al., 2011; Bastankhah and Porte-Agel, 2017; Meyer Forsting et al., 2023). Conversely, the effect of input turbulence on turbine blockage was shown to be insignificant when considering the entire wind farm (Meyer Forsting et al., 2023). In order to consider the unsteady nature of the turbulent flow upstream, a nonlinear dynamical model has recently been employed to forecast the average power output of the wind turbine (Wei and Dabiri, 2023).

The various studies mentioned above were mainly concerned with wind turbines. To the authors' knowledge, only a very limited number of studies have investigated changes in the turbulent flow in front of a horizontal axis tidal turbine (HATT). The contribution of the finite size of the domain to the blockage effect has been evaluated both numerically and experimentally (Kolekar et al., 2019; Zhang et al., 2021). This is referred to as the channel blockage effect, defined as the ratio of the experimental (or numerical) cross-sectional area to the rotor-swept area. In contrast, there is much less information about the flow changes resulting from a tidal turbine induction itself. Recently, Particle Image Velocimetry (PIV) measurements were carried out in a water flume tank to investigate turbulent flow changes upstream of a scaled HATT (Druault and Germain, 2022). Measurements made with and without the turbine allowed a comparison of turbulent flow characteristics. An important mean axial velocity deficit (around 30%) was observed in front of the hub regardless of the uniform or shear flow upstream. Globally, by analyzing the turbulent flow in the induction zone upstream, it was observed that the flow modifications were more marked just in front of the hub compared to those in front of the rotating blades (Druault and Germain, 2022). Furthermore, based on PIV measurements in front of an operating scaled HATT in uniform flow, Jouenne et al. (2023) analyzed the effect of the thrust coefficient (the rotational speed of the turbine) on the induction effect of the turbine. They also investigated the mean axial velocity deficit as a function of the thrust coefficient, allowing us to check the validity of selected analytical induction models currently used in the wind turbine context. The results showed that the reference self-similar model (Troldborg and Meyer Forsting, 2017) gave very good results upstream of the rotating blades, but had limitations upstream of the hub. They have then proposed to couple the current self-similar model to a model related to hub induction (Anderson et al., 2020), allowing to take into account the effects of both the hub and the rotating blades, separately. This has been validated for an incoming uniform flow (Jouenne et al., 2023).

To confirm those results, we propose in this work to examine the induction effects for various sheared flows that impact a turbine operating at several rotational speeds (several thrust coefficients). This will enable us to extend the validity of the coupled induction model by applying it to an incoming sheared flow. The remainder of the paper is organized as follows. In section 2, the experimental set-up and measurements method are presented. Section 3 proposes to analyze the TSR effect on the mean shear flow modifications in front of the turbine. The comparison between experimental data and analytical models is detailed in section 4. In section 5, a discussion is made to justify the need to differentiate hub and rotating blade blockage in tidal turbines by comparison with wind turbine applications.

2. Experimental set-up and measurements method

Details of the experiments including the experimental facility, the measurement method, and associated errors were reported in (Ikhennicheu, 2019; Ikhennicheu et al., 2019a; Druault and Germain, 2022). Here is only a brief description.

Measurements are carried out in the IFREMER (French Institute for the Exploitation of the Sea) wave and current circulation flume tank (Fig. 1) whose dimensions are $L_x \times L_y \times L_z = 18\,\mathrm{m}$ long $\times$ $4\,\mathrm{m}$ wide $\times$ $2\,\mathrm{m}$ high where (x, y, z) represent the axial, spanwise and vertical directions, respectively. The mean free stream velocity $U_\infty = 1\,\mathrm{m\,s^{-1}}$ is uniform, with a low turbulence intensity $I_\infty = 1.5\%$. A hydrodynamically smooth wall boundary layer (Ikhennicheu et al., 2019b; Ikhennicheu, 2019) is developed over the wall.

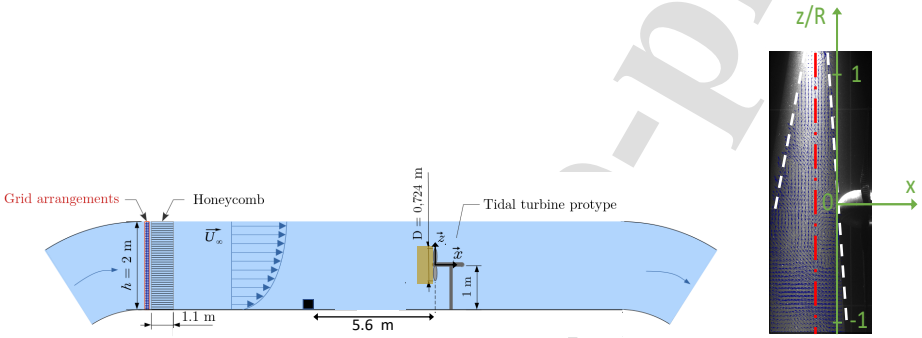

Figure 1: Left: Schematic view of the experimental setup including the wall-mounted obstacle and the PIV measurement plane (orange) in front of the operating turbine located in the position X_3. Right: Illustration of an instantaneous velocity vector field, to which is superimposed the vertical line (red) where instantaneous velocity vectors are extracted. The white dashed lines indicate the reduction of the measurement plane due to the triangular laser sheet and the shadow effect.

A 1:20 scaled three-blade horizontal axis tidal turbine (HATT) (Gaurier et al., 2017, 2020; Druault et al., 2022) with a diameter $D = 2 \times R = 0.724\,\mathrm{m}$ is centered mid-depth ($z = 0$) and mid-span ($y = 0$) in the flume tank (see Fig. 1). The diameter of the hub is $D_h = 2 \times R_h = 0.092\,\mathrm{m}$ therefore, the ratio of the hub to the turbine diameters is $D_h/D = 0.127$. The rotational speed of the turbine is controlled, and the pitch of the blade does not change. Three turbine operating configurations are considered, each with a different turbine rotational speed related to Tip Speed Ratios ($TSR = \omega R/U_\infty$, where ω is the angular rotational speed) of 3, 4, and 5. The nominal operating point corresponds to $TSR = 4$ (Magnier et al., 2020). Note that an experiment with a parked turbine (denoted $TSR0$) has also been carried out with a blade aligned along the upper vertical z axis. Each root of the blade is equipped to allow measurements of the thrust forces of the blade (T_b). The global thrust of the turbine T_t applied on the main rotational axis is also measured. These measurements, sampled at 120 Hz, are obtained simultaneously with Particle Image Velocimetry (PIV) measurements in front of the turbine.

The turbine is longitudinally placed in the wake of a wall-mounted square cylinder of height $H = 0.25\,\mathrm{m}$ and $6H$ long, which allows reproducing in situ Alderney Race shear flow conditions at scale (Sentchev et al., 2020b; Ikhennicheu, 2019). The obstacle is placed in the center of the test section, symmetrically around the span-wise origin $y = 0$ and the origin of the x axis is set at the center of the cylinder. The Reynolds number $Re = U_\infty H/\nu$ (with ν the water kinematic viscosity) is around 2.5×10^5, approaching the conditions in situ (Ikhennicheu et al., 2019b). Let us recall that in the Alderney Race

potential farm site, the axial mean velocity profile follows a power law:

$$U = U_{ref}\left(\frac{z}{D_e}\right)^{1/\alpha} \tag{1}$$

with α ranging from 4 to 14 (Sentchev et al., 2020a), U_{ref} a reference velocity, D_e the depth of water column, and z the distance from the bottom. In the following, the determination of α is done using the mean velocity at the mean depth in the shear part of the flow as U_{ref} and $D_e = 2\,\mathrm{m}$. The turbine is successively placed at three different locations in the wall-mounted cylinder wake: $(X_1,\ X_2,\ X_3) = (2.5,\ 4,\ 5.6)$m, corresponding to different shear velocity profiles that can be obtained at a specific site (Gaurier et al., 2020; Druault and Germain, 2022). Based on previous experiments (Ikhennicheu et al., 2020), an illustration of the mean axial velocity field deduced from the Reynolds decomposition is provided in figure 2 (left-hand side). The three sections (X_1, X_2, X_3) are indicated with vertical lines.

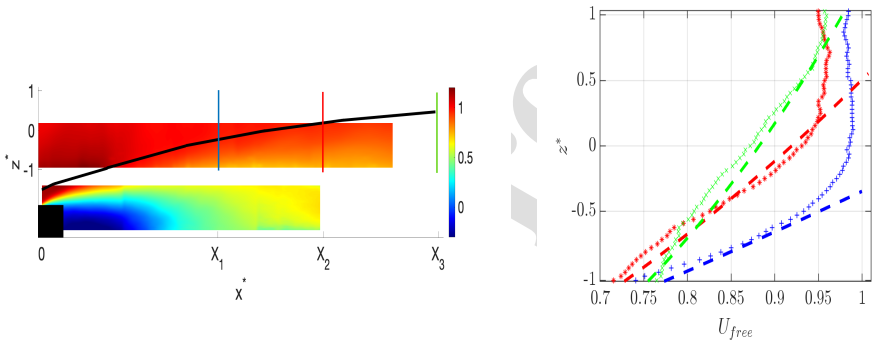

Figure 2: Left: Mean axial velocity component in the wall-mounted cylinder wake (Ikhennicheu et al., 2020). Right: The mean axial velocity component of the free flow U_{free} and its respective power-law estimation (dashed lines) at the three streamwise positions of interest. Blue $\times$: X_1, $z^{1/1.3}$; red $\circ$: X_2, $z^{1/2}$; green $+$: X_3, $z^{1/3}$.

For each streamwise position, planar Particle Image Velocimetry (PIV) measurements are conducted upstream of the turbine, in a vertical plane located at $y = 0$ (see Fig. 2). Due to the shadow effect (Jouenne et al., 2023), the instantaneous axial u and vertical w velocity components extracted along a vertical line at $0.07D = 0.05$m upstream of the hub extremity are only retained for analysis. The resulting velocity field is then sampled with $N_z = 74$ points that span a larger range than the diameter of the turbine, $-1.1 \leq z^* \leq 1.2$ with $z^* = z/R$. $N_t = 2700$ instantaneous vector fields sampled at $dt = 0.067\,\mathrm{s}$ (the PIV sampling frequency is 15 Hz) are obtained. PIV measurements are also carried out at the same X_i locations without the turbine to allow a comparison of the modifications of the velocity field due to the presence of the rotating turbine.

Figure 2 shows the superposition of the mean axial velocity profiles of the free flow, U_{free} for the three positions X. Three different types of sheared flows are observed:

1. X_1 position: the velocity profile follows the power law decay with $\alpha = 1.3$ in the lower half of the turbine, above the profile is uniform;
2. X_2 position: the velocity profile follows the power law decay with $\alpha = 2$ for $z^* \in [-1, 0.2]$, above the profile is uniform;
3. X_3 position: the velocity profile follows the power law decay with $\alpha = 3$ over the entire height of the turbine.

2.1. Thrust measurements

The total thrust of the turbine and the PIV velocity field measurements are carried out simultaneously in front of the turbine. The generally used definition of the turbine thrust coefficient C_t is:

$$C_t = \frac{T}{\frac{1}{2}\rho\pi R^2 \langle U \rangle^2} \tag{2}$$

where T is the time average of the thrust measurements and $\langle U \rangle$ is a reference velocity related to the flow upstream of the turbine induction area. In the presence of uniform flow, it is recommended to take a reference velocity at the hub height and at least two diameters upstream of the turbine. However, when the incoming shear flow is considered, such a velocity is not representative of the mean flow that really impacts the turbine. Similarly, in the presence of a rising flow in the water column, the usual definition of U_{ref} may not correspond at all to the flow that actually impacts the turbine (Druault and Germain, 2022). Several propositions (Meyer Forsting et al., 2018) have been formulated to determine an equivalent velocity $\langle U \rangle$ representative of the flow that actually affects the turbine. We have adopted the following definition: $\langle U \rangle = \langle U_{free} \rangle_z$, which corresponds to the spatial average along the diameter of the turbine (in the z direction) of the time-average axial velocity component measured in free flow.

However, as previously observed (Jouenne et al., 2023), the thrust coefficient related to only the thrust force of the three blades (denoted T_b) is preferentially used in the induction models. Taking into account the area swept by the blades, this coefficient is defined as follows.

$$C_{t_b} = \frac{T_b}{\frac{1}{2}\rho\pi \left(R^2 - R_h^2\right) \langle U \rangle^2} \tag{3}$$

Table 1 summarizes the corresponding estimated values of C_t and C_{t_b} for each flow configuration.

2.2. Flume tank blockage correction

In addition, a blockage correction method based on an actuator disk model is used to account for confinement-induced blockage (Sorensen, 2016; Bahaj et al., 2007). This method requires i) the blockage ratio, which is the ratio of the turbine area to the water flume tank cross-section area, $\pi R^2/(D_e \times L_y)$; ii) the thrust coefficients C_t as determined by (2). In this work, the turbine blockage is determined from the uniform flow U_∞. Indeed, the determination of the thrust coefficient C_t based on U_{free} already takes into account the wall cylinder blockage and therefore does not need to be considered again. Following the formulation given in Sorensen (2016) and Bahaj et al. (2007), an iterative calculation is performed to estimate the corrected values of C_t^{cor} (see Table 1). Note that such a formulation is not suitable when the C_t values are superior to 1.17, which is the case in (X_3-position - TSR5). In the last case, C_t^{cor} is set to 1. The corrected values will be used in the analytical models described below.

3. Tip-Speed Ratio (TSR) effect on the flow modifications ahead of the turbine

Our initial focus is on examining any alterations in the mean velocity field $U(z)$ estimated from the Reynolds average decomposition $u(z,t) = U(z) + u'(z,t)$, with $u'(z,t)$ the fluctuating part of the instantaneous component $u(z,t)$. In the following, the radius of the turbine R is used to normalize the spatial variables, e.g. $z^* = z/R$, and the polar coordinates ($r \in [0:R]$, $\theta = \pi/2, 3\pi/2$, with $r = 0$ at the hub center) is used to describe the vertical velocity profile that extends along the diameter of the turbine, that is, $z^* \in [-1:1]$.

	C_t	C_t^{cor}	C_{t_b}	$C_{t_b}^{cor}$
$x = 10$				
TSR3	0.80	0.77	0.74	0.71
TSR4	1.01	0.94	0.95	0.89
TSR5	1.12	0.99	1.05	0.96
$x = 16$				
TSR3	0.88	0.83	0.82	0.79
TSR4	1.06	0.97	1.02	0.94
TSR5	1.21	0.99	1.12	0.99
$x = 23$				
TSR3	0.92	0.87	0.85	0.81
TSR4	1.12	0.99	1.05	0.96
TSR5	1.22	1.00	1.14	0.99

Table 1: Turbine thrust coefficients C_t determined from thrust measurements for each flow configuration (equation 2). Turbine thrust corrected coefficients C_t^{cor} taking into account of the flume tank blockage.

Figure 3 shows the mean axial velocity component $U(z)$ along the normalized vertical direction z^* for the four flow configurations. Figure 4 gives a comparison of the percentage deficit calculated as $100 \times |U(z) - U_{free}(z)|/U_{free}(z)$ for each flow configuration.

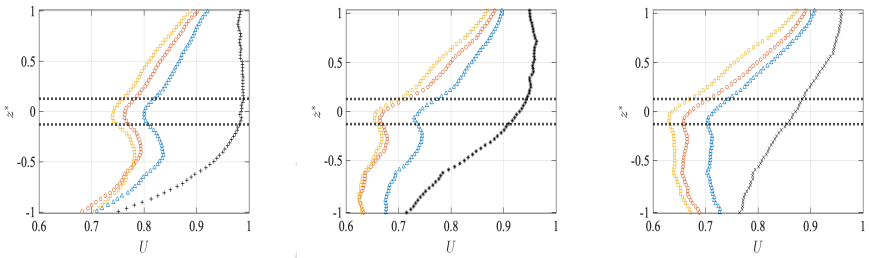

Figure 3: Comparison of the mean axial velocity profiles along the vertical turbine diameter. Black: free flow, blue △: TSR3, red ○: TSR4, yellow □: TSR5. From left to right: positions X_1, X_2, and X_3.

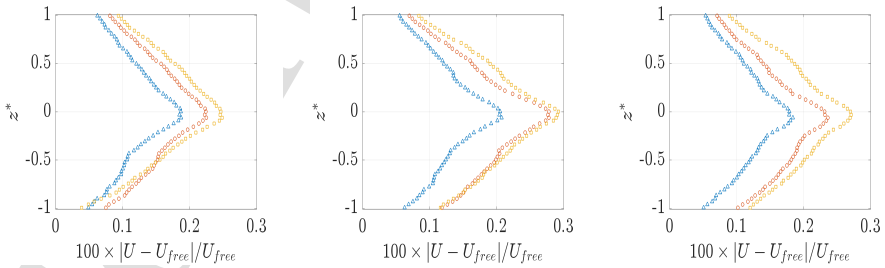

Figure 4: Comparison of the percentage velocity deficit $100 \times |U - U_{free}|/U_{free}$ along the vertical turbine diameter. From left to right: X_1, X_2, and X_3. The same symbols as for Fig. 3.

First, it is a confirmed fact that the turbine blockage increases in proportion to the

rotational speed, as previously observed (Chen and Liou, 2011; Kolekar and Banerjee, 2015). Second, the central position of the hub ($r = 0$) experiences the highest mean axial velocity deficit (between 18% -TSR3 and 29% -TSR5). This finding is again consistent with previous studies on wind turbines, regardless of the type of incoming flows (Bastankhah and Porte-Agel, 2017; Howard and Guala, 2015; Medici et al., 2011; Simley et al., 2016; García Regodeseves and Santolaria Morros, 2021). Also, the percentage deficit values are in agreement with those obtained for a uniform flow that impacts a tidal turbine (Jouenne et al., 2023). Third, when a uniform upstream flow is considered, the mean axial velocity field $U(z)$ ahead of the turbine is symmetric about the hub (Druault and Germain, 2022; Jouenne et al., 2023). On the contrary, in the case of an incoming shear flow, $U(z)$ becomes skewed and asymmetric and the degree of asymmetry is determined by the characteristics of the incoming shear velocity profiles, as discussed below.

It is interesting to note that the mean axial velocity deficits are almost of the same amplitude at the tips of the blade ($z^* = \pm 1$) in the case of the lowest turbine rotational speed (TSR3). But, when increasing the turbine rotational speed (TSR4 and TSR5 cases), the mean axial velocity deficits are more pronounced on the lower side of the hub ($z^* = -1$) than on the upper side of the hub ($z^* = 1$). The lowest axial velocity part of the shear flow is more affected by the increasing blockage effect induced by the increasing turbine rotational speed and so the perceived solidity. This should be related to the characteristic time of transfer of momentum from the axial component to the radial component through the sweeping process of the turbine rotation.

Although the percentage velocity deficit and the absolute velocity deficit above the hub exhibit quasi-similar profiles with respect to the turbine rotational speed and positions X, changes in the absolute velocity deficit profiles below the hub should be emphasized. When α is low (position X_1), the maximum value of the mean axial velocity in the lower part ($z^* < 0$) is obtained around $z^* = -0.5$ as the result of the competition between two opposite shear velocity profiles (the second one developing from the hub). This particular profile may have noticeable impacts when considering the differential local constraints that act on the blades. When α increases otherwise, as for the positions X_2 and X_3 in which the incoming shear flow extends the diameter of the turbine, the maximum of the mean axial velocity in the lower part ($z^* < 0$) is shifted upward and is barely visible in the latter case.

Recently, it was observed that for a fixed TSR, the percentage of velocity deficit remains globally constant regardless of the nature of the incoming flow (Druault and Germain, 2022). Present results confirm that the rotational speed of the turbine primarily governs the percentage deficit. Thus, the deceleration decreases with the thrust coefficient, but the overall shape of the mean axial velocity profiles remains unchanged in the proximity of the rotor.

The changes in the mean vertical velocity component are now analyzed. Note that the absolute value of the vertical velocity component W corresponds to the radial velocity component U_r, which is represented in Figures 5 as a function of the coordinate z^* to better highlight the expansion of the flow around the turbine. The test case TSR0 is also represented to highlight the rotational effect of the blade on U_r, especially in the zoomed-in view around the hub.

We can observe that the free flow has a non-null vertical velocity component W that decreases in a quasi-linear fashion with the vertical direction z. This slight variation from the uniform flow is associated with the rising wake flow (Ikhennicheu et al., 2019b).
As expected, the mean radial velocity component U_r ahead of the rotor increases with the radial distance r and the turbine rotational speed due to flow expansion. At each position X, the maximum of U_r is obtained symmetrically around $r = \pm 0.9R$, which is

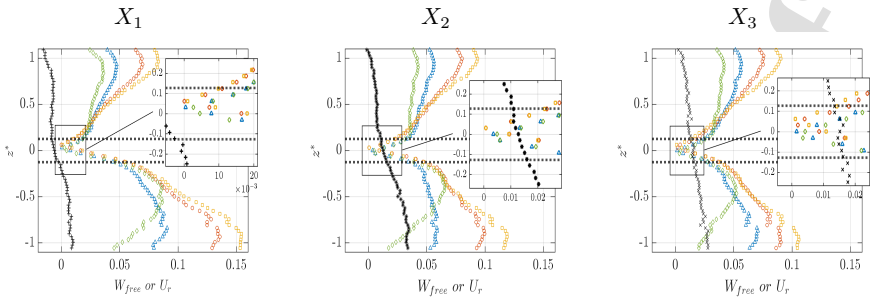

Figure 5: Comparison of the mean radial velocity profile along the vertical turbine diameter superimposed onto the vertical W_{free} velocity component. From left to right: X_1, X_2, and X_3. Black: free flow, green ◊: TSR0, blue △: TSR3, red ○: TSR4, yellow □: TSR5. The insert shows a zoomed view around the hub.

consistent with previous observations (Medici et al., 2011). This specific radial position corresponds to the initiation of the tip vortex. Thus, as the mean radial velocity increases at the tip of the blade when the TSR increases, the intensity of the tip vortex generated at the tip of the blades will then be all the greater.

Small but persistent differences are observed in the vertical position of the minimum of U_r. When the turbine is at rest (TSR0), $U_r = 0$ is obtained along the hub axis. But when the TSR increases, $U_r = 0$ is slightly shifted upwards. The coupled mechanisms between the rotation of the hub and the incoming coupled (U_{free}, W_{free}) profile are certainly at the origin of this shift. Further investigations such as three-dimensional numerical simulations are needed to explain these complex mechanisms.

4. Comparison between modeling and experimental induction assessments

Different models exist to estimate the mean velocity field upstream of a turbine in operation. Although these models were originally developed for wind turbines (Branlard et al., 2020), we have recently used some of them for tidal turbines (Jouenne et al., 2023). We choose to focus only on the self-similar induction model (Troldborg and Meyer Forsting, 2017) and its recently derived version (Meyer Forsting et al., 2023). They are briefly described in the next section.

4.1. Self-similar induction models

Assuming a uniform axial mean flow U_∞, in the turbine induction area, the mean axial velocity $U(r, x)$ is estimated as follows:

$$U(r, x) = U_\infty - U_b^{v17}(r, x) \tag{4}$$

where $U_b^{v17}(r, x)$ corresponds to the absolute blockage loss estimated by the self-similar model 2017 version (Troldborg and Meyer Forsting, 2017):

$$U_b^{v17}(r, x) = a_0 U_\infty \left(1 + \frac{x}{\sqrt{R^2 + x^2}}\right) \mathrm{sech}^{\alpha_1}(\beta\varepsilon) \tag{5}$$

with a_0 the axial induction factor in the rotor

$$a_0 = \frac{1}{2}(1 - \sqrt{1 - \gamma C_T})$$

and

$$\varepsilon = \frac{r}{R\sqrt{\lambda(\eta + \frac{x^2}{R^2})}}.$$

The values of the constants have been set as follows: $\gamma = 1.1$, $\beta = \sqrt{2}$, $\alpha_1 = 8/9$, $\lambda = 0.587$ and $\eta = 1.32$. This model was designed and validated with more than 100 Reynolds Averaged Navier-Stokes (RANS) simulations of the air flow developing over a porous disk subjected to uniform flow U_∞.

Recently, a new version (denoted $v23$) of the self-similar model was proposed to better capture the induction generated by a wind farm (Meyer Forsting et al., 2023):

$$U_b^{v23}(r,x) = a_{0_n} U_\infty \left(1 + \frac{x}{\sqrt{R^2 + x^2}}\right) \mathrm{sech}^\alpha(\beta\varepsilon_n) \tag{6}$$

with

$$\varepsilon_n = -0.672\frac{x}{R} + 0.4897$$

and

$$a_{0_n} = \frac{1}{2}(1 - \sqrt{1 - \gamma_n C_T})$$

in which γ_n is linearly dependent on the thrust coefficient, as established by RANS simulations, and it may undoubtedly depend on the turbine characteristics. In this study, it is not feasible to regain the reliance, which requires the utilization of the parameters specified in the original paper.

4.2. Accounting for the non-uniformity of the upstream flow

In order to better account for the non-uniformity of the upstream flow, we propose two alternatives to the self-similar induction models. The first alternative consists of substituting U_∞ in (4) with the local velocity profile $U_{free}(r,x)$ free of any turbine, as measured in our study at each position X_i, to take into account the local shear velocity profile. This alternative leads to the following equation:

$$U(r,x) = U_{free}(r,x) - \frac{U_{free}(r,x)}{U_\infty} U_b(r,x) \tag{7}$$

The second alternative proposes using the spatial average velocity $\langle U \rangle$, already used to calculate the thrust coefficient (2) involved in (5) and (6), as a representative mean velocity of what the turbine perceives. This leads to the following equation:

$$U(r,x) = U_{free}(r,x) - \frac{\langle U \rangle}{U_\infty} U_b(r,x) \tag{8}$$

When analyzing the effect of the velocity taken as reference in model formulations (7) or (8), the spatial average velocity $\langle U \rangle$ appears to be more appropriate. The associated results are closer to the experimental results than when equation (7) is used. This is certainly directly related to the fact that the thrust coefficient is also associated with spatially averaged forces. Therefore, we will use the formulation (8) in the following.

4.3. Comparison with experimental results

Figure 6 shows a comparison of the evaluation of the $v17$ and $v23$ models with the mean axial velocity measurements at one position X_1 and for two TSR values (TSR3 and TSR4). The thrust coefficient C_t is determined from (2) and (3). As expected, when the total thrust of the turbine is used, the velocity deficit is greater than the one calculated

from the thrust of the three blades. In each case, similar velocity profiles are obtained; only a difference related to the amplitude of these velocities is observable in relation to the values of the thrust coefficient. The new $v23$ model increases the perceived velocity deficit upstream of the turbine, which is consistent with previous results since this model was originally developed to take into account the interaction of the turbines in a wind farm (Meyer Forsting et al., 2023). Therefore, the empirical parameters used for this new model may not be optimized for the current tidal turbine and the experimental conditions in the confined flume tank. In contrast, the original $v17$ model was calibrated for a single wind turbine. Therefore, we will use the former $v17$ model in the remainder of this study, as it appears to be more relevant to our practical configuration.

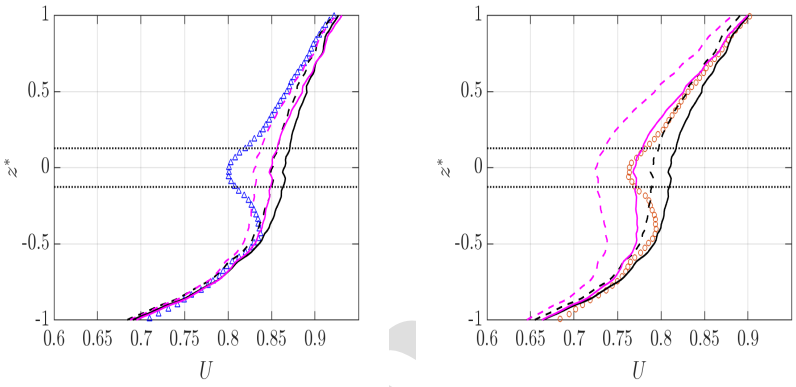

Figure 6: Comparison of $v17$ (black) and $v23$ (magenta) analytical models to the experimental mean axial velocity component for two TSRs (TSR3-left and TSR4-right) at X_1 position. Both models use C_t values computed from equation 2 (dashed lines) or equation 3 (lines). The hub radius is marked with black dotted lines.

Figure 7 shows a comparison of the evaluation of the $v17$ model with the mean axial velocity measurements at the three positions X_i and for the three TSR values (TSR3, TSR4, and TSR5). The thrust coefficient C_t is determined from equation (2) or equation (3).

Near the tip of the blade ($r/R > 0.5$), the estimate of the $v17$ model compares fairly well to the experimental results regardless of the free flow and the determination of the thrust coefficient. The largest deviations are clearly visible in the region ahead of the hub ($z^* < R_h$). This confirms previous observations made for tidal turbines that are subject to uniform flow (Jouenne et al., 2023). Consequently, as suggested by Jouenne et al. (2023), one proposes to couple previous analytical model to another analytical model devoted to the hub and described in the next section.

4.4. Hub modeling

Anderson et al. (2020) have recently examined the nacelle blockage effect in wind turbine and its consequences on the turbine wake flow and on the turbine loading. To access such an effect, they proposed a simplified analytical model that reproduces a two-dimensional steady-velocity field developing around a hub. It allows modeling of the mean axial and radial velocity fields upstream and downstream of a hub. The hub is viewed as an ellipsoid of eccentricity e and of semi-axes of revolution a_x (along x) and a_r (along r). The reader is referred to the original paper for mathematical development. Here, we only

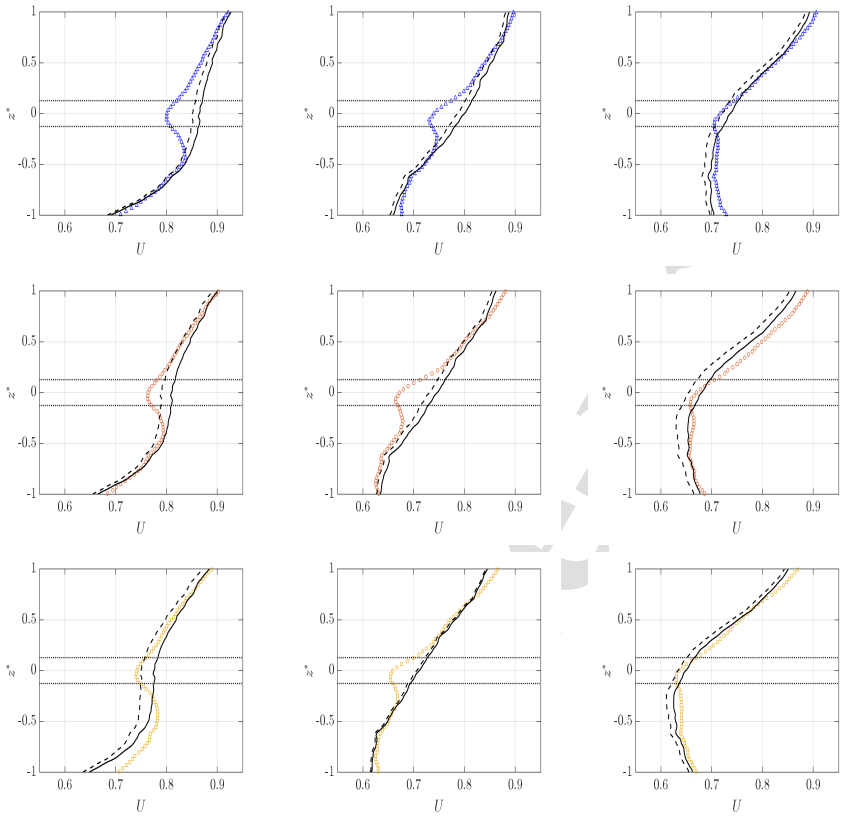

Figure 7: Comparison of the $v17$ analytical model to the experimental mean axial velocity component for the nine test cases. The $v17$ model uses C_t values computed from equation 2 (lines) or equation 3 (dashed lines). The hub radius is marked with black dotted lines. Columns (left to right): X_1, X_2 and X_3-positions. Rows (top to bottom): TSR3, TSR4, TSR5.

recall the main equations used to analytically access the mean axial and radial velocity field $(U_{hub}(x,r), U_{rhub}(x,r))$ around the hub subjected to a uniform velocity, U_∞:

$$U(x,r) = U_\infty - U_{hub}(x,r) = U_\infty - \frac{\partial\phi}{\partial\mu}\frac{\partial\mu}{\partial x} - \frac{\partial\phi}{\partial\xi}\frac{\partial\xi}{\partial x} \tag{9}$$

$$U_{rhub}(x,r) = -\frac{\partial\phi}{\partial r} = -\frac{\partial\phi}{\partial\mu}\frac{\partial\mu}{\partial r} - \frac{\partial\phi}{\partial\zeta}\frac{\partial\zeta}{\partial r} \tag{10}$$

where ϕ is the potential velocity and (μ, ζ) the semi-elliptic coordinates as defined in (Anderson et al., 2020).
For the present application U_∞ is replaced by $U_{free}(r, X_i)$, with $i = 1, 2, 3$.
Note that in the hub model formulation, the turbine thrust does not appear explicitly as well as the effects of blade rotations.

4.5. Coupled models for tidal turbine induction

An enhancement of the self-similar model is to consider the effect of hub blockage that was not accurately modeled for tidal turbine applications. To do this, an extra

contribution to the absolute blockage loss is added to the original self-similar model to account for the obstruction by the hub alone. We then propose the following formulation of the modified self-similar model, accounting for both the non-uniformity of the upstream flow and the blockage loss induced by a hub of large aspect ratio relative to the turbine diameter:

$$U(r,x) = U_{free}(r,x) - \frac{\langle U \rangle}{U_\infty} U_b(r,x) - U_{hub}(r,x) \tag{11}$$

The evaluation of the proposed model is compared with the experimental results in figure 8 and the associated relative errors computed as:

$$E(r,x) = |U(r,x)_{mod} - U(r,x)_{exp}| / U(r,x)_{exp} \tag{12}$$

are represented in figure 9 for the nine flow configurations.

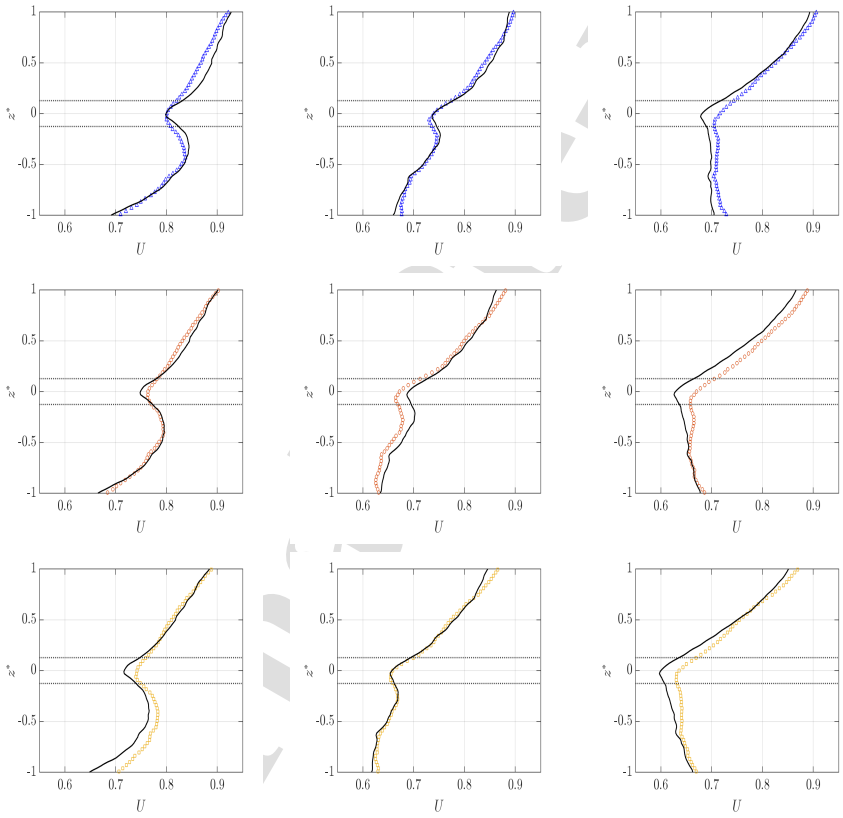

Figure 8: Comparison of the modified self-similar model (11) evaluation to the experimental mean axial velocity component. The vertical extent of the hub is delimited with black dotted lines. Columns (left to right): X_1, X_2 and X_3-positions. Rows (top to bottom): TSR3, TSR4, TSR5.

Overall, the estimated upstream velocity profiles compare fairly well with the experiments in every case. Errors are of low amplitude (less than 5%) which is close to the order of magnitude of the measurement errors (Ikhennicheu, 2019). Therefore, the addition of the hub contribution to the total blockage loss significantly improves the results. Small nuances regarding the position of the evaluation will be discussed below.

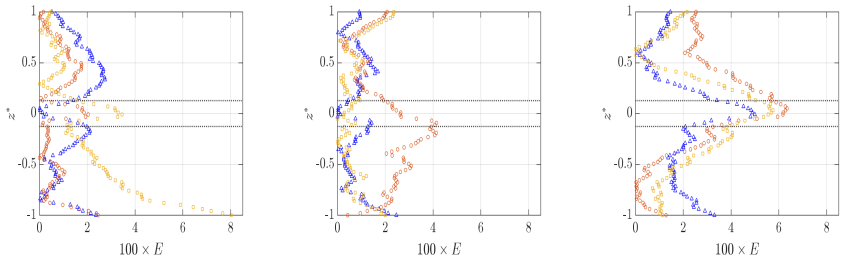

Figure 9: Errors between model results and experimental data. The vertical extend of the hub is delimited with black dotted lines. From left to right: X_1, X_2 and X_3-positions.

When the shear profile spans the entire turbine area (X_3 location), the maximal errors are systematically observed ahead of the hub, as shown in figure 9, right-hand side. As this systematic error could *a priori* be related to some limitations in the hub blockage loss model for which the blade rotation is not taken into account, we believe that it could also be related to an inherent bias in the self-similar model in which a unique global thrust coefficient is used. This systematic error is not observed when the shear profile spans a fraction of the turbine area (X_1 and X_2 locations). In position X_1 for example, where the freestream velocity profile is uniform in the upper part of the turbine ($z^* > 0$) and sheared in the lower part ($z^* < 0$), errors do not exceed 3% throughout the diameter of the turbine, except for the case $TSR5$ near the bottom tip of the blade. This singular behavior might have different origins. Again, it could be related to the unique global thrust coefficient (therefore independent of the vertical coordinate) used in the self-similar model that cannot correctly represent the forces perceived by the blades over their entire surface. One solution to improve this could be to inject local thrust coefficient values into the model that would be a function of (z, r). Or, it could be related to the asymmetric velocity deficit already observed when increasing the turbine rotational speed. In either case, complementary studies should be performed to elucidate this point. Indeed, the level of this error (of the order of the measurement error) and the fact that the maximum error in the position X_2 is obtained for TSR4 do not enable us to draw a clear interpretation here.

5. Discussion and Conclusion

It has been confirmed that to accurately model the velocity deficit upstream of a tidal turbine, hub blockage must be considered. It was previously highlighted in the context of a uniform upstream flow (Jouenne et al., 2023), and it is now further evidenced in the context of an upstream shear flow.

This is achieved by incorporating a local extra velocity deficit model into the self-similar model specifically designed for wind turbines. In the original approach, the impact of hub blockage was not explicitly considered. This is generally justifiable in the case of a large wind turbine whose ratio between the hub and the rotor radii ranges from 4% to 5%. But, when the typical ratio between the hub and the diameter of the rotor for tidal turbines is around $12 - 15\%$ or greater (Wani and Polinder , 2017; Dufour et al., 2022), the hub is a significant obstacle that must be taken into account in a blockage loss model. A large hub reduces the area available for the flow, resulting in a noticeable increase in the axial velocity in front of the blades. It certainly also changes the angle of attack of the blade section, modifying the local thrust force in this area.

To isolate the thrust force of the hub, Table 2 shows the experimental values obtained by subtracting the thrust force of each blade from the total thrust of the turbine. The thrust of the hub contributes between 7% and 9% of the total turbine thrust, which is significant.

Taking into account the effects of the hub has already been mentioned in a previous study (Bontempo and Manna, 2019) dealing with small wind turbines. In this case, the ratio between the hub and rotor radii is around $25\% - 30\%$. It has been shown that taking into account the effects of hub blockage was necessary to better represent the turbine wake flow.

	$x^* = 10$			$x^* = 16$			$x^* = 23$		
	TSR3	TSR4	TSR5	TSR3	TSR4	TSR5	TSR3	TSR4	TSR5
T_{hub}/T (%)	9.0	7.8	7.3	7.8	6.9	6.7	8.7	7.8	7.4

Table 2: Ratio of the hub thrust to the total turbine thrust.

To conclude, the investigation of the turbine induction in a shear flow is of great interest because in-situ the turbines spend most of their life time in non-uniform shear tidal current due to bathymetry effect or/and to the turbine wake flow in a tidal farm. By performing velocity measurements in front of a rotating turbine subjected to different sheared flows, we were able to determine the changes in the mean velocity field as a function of the rotation speed of the turbine, as well as the nature of the sheared axial velocity profile.

The experimental measurements were then compared to numerical results deduced from analytical induction models based on crude assumptions. Overall, the experimental and analytical results compare fairly well regardless of the turbine rotational speed and/or the nature of the incoming shear velocity profile. However, the present results show that in the presence of sheared flow, such a simplified modeling (such as the self-similar model) may not always be really suitable to correctly estimate the velocity deficit upstream of the turbine. Although this model is still the most used and popular one for the induction analysis of horizontal axis wind turbines, it was calibrated using the simple actuator disk method. This model is also based on an average thrust coefficient assuming that the velocity deficit remains globally similar throughout the water column. However, the thrust forces vary as a function of the position in the water column, depending locally on the different incoming velocity values. These forces also vary along the radial coordinates linked to the blade profile. Thus, in the presence of sheared flow, it would be preferable to integrate the spatially local dependence on the thrust coefficient into the formulation of this model.

Furthermore, the results showed that an accurate characterization of the induction effects of a tidal turbine requires adding the hub blockage effects to those of rotating blades. A new analytical induction model is then proposed that combines both the models related to the rotating blade and the hub. The proposed coupled analytical induction model better predicts the mean flow deficit in front of the tidal turbine and no more 5% of errors are observed between analytical and experimental results.

Adding the hub blockage effects to those of rotating blades seems specific to tidal turbines or small-sized wind turbines. The main parameter justifying the use of this coupled model is the ratio between the hub and the rotor radii. It is recommended to couple both models when the ratio is superior to at least 10%. This result is therefore very important for the numerical modeling of the flow around tidal turbine, especially in the case of tidal-farms where the specific induction effect of hub must certainly be taken into account.

Acknowledgements

This research was partly funded by the Region Hauts-de-France in the framework of the project CPER 2021-2027 IDEAL. The authors would like to gratefully acknowledge Maria Ikhennicheu and Benoît Gaurier involved in the experimental database generation and to warmly thank Thomas Bacchetti and Jean-Valery Facq for their assistance and precious advices.

CRediT authorship contribution statement

Philippe Druault: Data analysis, software, writing-original draft, review and editing. **Jean-François Krawczynski**: Data analysis, writing-original draft, review and editing. **Erdi Çan**: Sofware, data analysis. **Grégory Germain**: Conceptualization, Funding acquisition, writing- review and editing.

References

Anderson, B., Branlard, E., Vijayakumar, G., Johnson, N., 2020. Investigation of the nacelle blockage effect for a downwind turbine. J. Phys.: Conf. Ser. 1618.

Bahaj, A.S., Molland, A.F., Chaplin, J.R., Batten, W.M.J., 2007. Power and thrust measurements of marine current turbines under various hydrodynamic flow conditions in a cavitation tunnel and a towing tank. Renewable Energy 32, 407–426.

Bastankhah, M., Porte-Agel, F., 2017. Wind tunnel study of the wind turbine interaction with a boundary-layer flow: Upwind region, turbine performance, and wake region. Phys. Fluids 29, 065105.

Bontempo, R., Manna, M., 2019. A ring-vortex actuator disk method for wind turbines including hub effects. Energy Conversion and Management 195, 672–681.

Branlard, E., Gaunaa, M., 2015. Cylindrical vortex wake model: right cylinder. Wind Energy 18, 1973–1987.

Branlard, E., Meyer Forsting, A., 2020. Assessing the blockage effect of wind turbines and wind farms using an analytical vortex model. Wind Energy 23, 2068–2086.

Branlard, E., Quon, E., Meyer Forsting, A.Forsting, A., King, J., Moriarty, P., 2020. Wind farm blockage effects: comparison of different engineering models. Journal of Physics: Conference Series 1618, 062036.

Chen, T., Liou, L., 2011. Blockage corrections in wind tunnel tests of small horizontal-axis wind turbines. Exp. Thermal Fluid Science 35, 565–569.

Druault, P., Gaurier, B., Germain, G., 2022. Spatial integration effect on velocity spectrum: Towards an interpretation of the $-11/3$ power law observed in the spectra of turbine outputs. Renewable Energy 181, 1062–1080.

Druault, P., Germain, G., 2022. Experimental investigation of the upstream turbulent flow modifications in front of a scaled tidal turbine. Renewable Energy 196, 1204–1217.

Dufour, A., Gaurier, B., Pinon, G., Germain, G., Facq, J., Togneri, M., Represas, F., Nicolas, E., Marcille, J., 2022. Comparison of the experimental response of two horizontal axis tidal turbines to wave and current, in: Congrès Français de Mécanique.

García Regodeseves, P., Santolaria Morros, C., 2021. Numerical study on the aerodynamics of an experimental wind turbine: Influence of nacelle and tower on the blades and near-wake. Energy Conversion and Management 237, 114110.

Gaurier, B., Druault, P., Ikhennicheu, M., Germain, G., 2020. Experimental analysis of the shear flow effect on tidal turbine blade root force from three-dimensional mean flow reconstruction. Philosophical Transactions of the Royal Society A: Mathematical, Physical and Engineering Sciences 378.

Gaurier, B., Germain, G., Facq, J.V., 2017. Experimental study of the Marine Current Turbine behaviour submitted to macro-particle impacts, in: 12th European Wave and Tidal Energy Conference, Cork, Ireland.

Howard, K., Guala, M., 2015. Upwind preview to a horizontal axis wind turbine: a wind tunnel and field-scale study. Wind Energy 19, 1371–1389.

Ikhennicheu, M., Druault, P., Gaurier, B., Germain, G., 2020. Turbulent kinetic energy budget in a wall-mounted cylinder wake using PIV measurements. Ocean Engineering 210, 107582.

Ikhennicheu, M., 2019. Étude expérimentale de la turbulence dans les zones à forts courants et de son impact sur les hydroliennes. Ph.D. thesis. Université de Lille.

Ikhennicheu, M., Germain, G., Druault, P., Gaurier, B., 2019a. Experimental investigation of the turbulent wake past real seabed elements for velocity variations characterization in the water column. International Journal of Heat and Fluid Flow 78, 108426.

Ikhennicheu, M., Germain, G., Druault, P., Gaurier, B., 2019b. Experimental study of coherent flow structures past a wall-mounted square cylinder. Ocean Engineering 182, 137–146.

Jouenne, L., Druault, P., Krawczynski, J.F., Germain, G., 2023. Induction study of a horizontal axis tidal turbine: Analytical models compared with experimental results. Ocean Eng. 268.

Keane, A., Nisbet, I., Calvo, G., Pickering, G., Tulloch, J., More, G., Koronka, N., 2022. Wind farm cumulative induction zone effect and the impact on energy yield estimation. Renewable Energy 181, 1209–1222.

Kolekar, N., Banerjee, A., 2015. Performance characterization and placement of a marine hydrokinetic turbine in a tidal channel under boundary proximity and blockage effects. Applied Energy 148, 121–133.

Kolekar, N., Vinod, A., Banerjee, A., 2019. On blockage effects for a tidal turbine in free surface proximity. Energies 12, 3325.

Li, C., Abraham, A., Li, B., Hong, J., 2020. Incoming flow measurements of a utility-scale wind turbine using super-large-scale particle image velocimetry. J. Wind Eng. Ind. Aerodynamics 197, 104074.

Magnier, M., Druault, P., Gaurier, B., Germain, G., 2020. Comparison of bathymetry variation effects on tidal turbine behaviour, in: 17èmes journées de l'hydrodynamique, Cherbourg, France.

Medici, D., Ivanell, S., Dahlberg, J.Å., Alfredsson, P.H., 2011. The upstream flow of a wind turbine: blockage effect. Wind Energy 14, 691–697.

Meyer Forsting, A., Van der Laan, M., Troldborg, N., 2018. The induction zone/factor and sheared inflow: A linear connection ? Journal of Physics: Conference Series 1037, 072031.

Meyer Forsting, A., Navarro Diaz, G., Segalini, A., Andersen, S., Ivanell, S., 2023. On the accuracy of predicting wind-farm blockage. Renewable Energy 214, 114–129.

Segalini, A., 2021. An analytical model of wind-farm blockage. J. Renewable Sustainable Energy 13.

Sentchev, A., Nguyen, T.D., Furgerot, L., Bailly du Bois, P., 2020a. Underway velocity measurements in the Alderney Race: towards a three-dimensional representation of tidal motions. Philosophical transactions. Series A, Mathematical, physical, and engineering sciences 378, 20190491.

Sentchev, A., Thiébot, J., P.M., Bennis, A., 2020b. Theme Issue: New insights on tidal dynamics and tidal energy harvesting in the Alderney Race. Phil. Trans. Royal Society A.

Simley, E., Angelou, N., Mikkelsen, T., Sjöholm, M., Mann, J., Pao, L.Y., 2016. Characterization of wind velocities in the upstream induction zone of a wind turbine using scanning continuous-wave lidars. Journal of Renewable and Sustainable Energy 8.

Sorensen, J., 2016. General Momentum Theory for Horizontal Axis Wind Turbines. Springer.

Troldborg, N., Meyer Forsting, A., 2017. A simple model of the wind turbine induction zone derived from numerical simulations. Wind Energy 20, 2011–2020.

Wani, F., Polinder, H., 2017. A Review of Tidal Current Turbine Technology: Present and Future, in: 12th European Wave and Tidal Energy Conference, Cork, Ireland.

Wei, N., Dabiri, J., 2023. Power-generation enhancements and upstream flow properties of turbines in unsteady inflow conditions. J. Fluid Mech. 966.

Zhang, Y., Zhang, Z., Zheng, J., Zhang, J., Zheng, Y., Zang, W., Lin, X., Fernandez-Rodriguez, E., 2021. Experimental investigation into effects of boundary proximity and blockage on horizontal-axis tidal turbine wake. Ocean Engineering 225.

Zhang, Y., Shek, JKH., Mueller, MA., 2023. Controller design for a tidal turbine array, considering both power and loads aspects. Renewable Energy 216, 119063.

Highlights

- Tidal turbine blockage analysis for various thrust values and incoming shear flows
- Modified wind turbine induction model for large hub-to-turbine diameter ratio
- Development of a hybrid analytical tidal turbine induction model
- The model separately considers the action of the hub and the rotating blades
- The new model and experimental data showed good agreement regardless of turbine speed

Declaration of interests

☒ The authors declare that they have no known competing financial interests or personal relationships that could have appeared to influence the work reported in this paper.

☐ The authors declare the following financial interests/personal relationships which may be considered as potential competing interests: